Turbulent Friction Drag Reduction Using Electroactive Polymer & Electromagnetically-driven Surfaces

Kevin Gouder · Mark Potter · Jonathan F. Morrison

Abstract This work reports aerodynamic testing of two spanwise-oscillating surfaces fabricated out of electroactive polymers (EAPs) in the dielectric form of actuation (DEA), and of an electromagnetic-driven linear motor. Hot-wire and PIV measurements of velocity and direct measurement of friction drag using a drag balance are presented. A maximum of 16% surface friction reduction, as calculated by the diminution of the wall-normal streamwise velocity gradient was obtained. Among other quantities, the spatial dependence of the drag reduction was investigated. When this spatial transient and portions which are static are accounted for, the direct drag measurements complement the hot-wire data. PIV measurements where the laser beam was parallel to the oscillating surface at $y^+ \approx 15$, support the hot-wire data. The two actuators are original in design and significant contributions have been made to the development of EAPs. This experiment is the first to aerodynamically test EAP actuators at such a large scale and at a relatively moderate Re.

Keywords Electroactive Polymer · EAP · Friction Drag Reduction · Spanwise Oscillating Surface · Spanwise Travelling Wave

1 Introduction

This work reports progress made in the development and aerodynamic testing of technologies that could eventually enable the fabrication of a flexible wall able to

Kevin Gouder
Department of Aeronautics, Imperial College, London SW7 2AZ, UK
Tel.: +44 20 759 45141
Fax: +44 20 759 41974
E-mail: kevin.gouder04@imperial.ac.uk

execute local in-plane accelerations forming a spanwise travelling surface wave as proposed by Zhao et al (2004), or the recently proposed streamwise travelling wave of spanwise wall velocity, Quadrio et al (2009). Such techniques where the surface accelerations are local rather than global (as is a spanwise-oscillating wall) are more readily deployable in an engineering application. In anticipation of fabricating such a surface, two precursor surfaces were developed: both executing in-plane spanwise oscillations but based on two different technologies, one using EAP in DEA mode, and the other using an electromagnetic linear motor-driver.

Experiments (e.g. Bradshaw and Pontikos (1985), Laadhari et al (1994), Choi et al (1998)) and simulations (e.g. Jung et al (1992), Quadrio and Ricco (2004), Zhao et al (2004)) had shown that an initially fully developed two-dimensional boundary layer subjected to sudden spanwise forcing, exhibits a decrease in Reynolds shear stresses and turbulent friction drag. In most studies the forcing was wall-based, e.g. spanwise wall oscillations, spanwise travelling Lorentz forcing or spanwise travelling waves of an in-plane flexible wall. A reduction in the streamwise wall shear stress $\tau_w = \mu \frac{\partial U}{\partial y}$ through a reduction in $\frac{\partial U}{\partial y}$ within $y^+ = yu_\tau/\nu = 10$, (where y is the wall-normal coordinate, $u_\tau = \sqrt{\tau_w/\rho}$ is the friction velocity and, μ and ν are the dynamic and kinematic viscosities), was widely reported, e.g. Choi (2002). When normalised by u_τ of the unactuated case, the velocity and its gradient reduce within the linear sublayer and collapse further out beyond the depth of penetration of the disturbance. A common observation in these studies is a substantial reduction in turbulence intensity and the moving of its peak away from the wall.

The skewness and kurtosis wall-normal distributions of streamwise velocity fluctuations u, were investigated

by Quadrio and Sibilla (2000), who showed that the wall oscillation enhances some high-speed streaks while the elongated low-speed streaks are weakened resulting in an increased skewness. An increase in kurtosis in the viscous sublayer, suggesting an increase in intermittency was also reported, Il-Choi et al (2002). There has, however, been disagreement on the cause of the increase in skewness, whether it is through the increase in the intermittent large positive u, Choi and Clayton (2001), or through the reduction of small negative u, Il-Choi et al (2002), Quadrio and Sibilla (2000).

Addressing the changes in the frequency spectrum of u due to wall oscillations, Choi (2002) demonstrated that velocity fluctuations close to the wall are modulated by the wall motion and spikes at the oscillation frequency and its harmonics appear in their spectrum. Choi (2002) suggests the changes are consistent with energy transfer from large to small-scale eddies but Schoppa and Hussain (1998) suggest the suppression/augmentation of instability mechanisms.

The acceleration phase of the wall oscillation is an important factor responsible for the observed physical changes. Jung et al (1992) attributed reductions in Reynolds shear stress to the sudden transverse strain, in contrast with a constant imposed spanwise pressure gradient where the reduction in turbulence activity was temporary. This has been supported by Zhao et al (2004) who noted that while the input power required to move the wall transversally is in proportion to wall velocity, the extent of the control effect depends on wall acceleration. Akhavan et al (1993), Quadrio and Ricco (2003) claimed that the continuous relative shift between the near-wall streamwise vortices and the streaks prevents the turbulence from ever reaching an equilibrium state.

A variation of the spanwise-oscillating wall technique is the spanwise travelling wave (of finite wavelength in contrast to the infinite wavelength of wall oscillations) of body forcing such as the DNS of Du et al (2002) where differences between the two techniques were reported. Turbulence statistics for both techniques were similar but whereas travelling-wave excitation caused the disappearance of streaks, spanwise wall oscillations merely inclined them to the streamwise direction. A more recent variation was suggested in the DNS of Quadrio et al (2009), where the wall was made to execute sinusoidal waves of spanwise velocity travelling along the streamwise direction. This followed from Quadrio et al (2007) who had imposed a spatial sinusoidal distribution of spanwise velocity over a wavelength λ_x but added a phase speed c to this distribution. This enabled the distribution to be made to travel backwards (where drag reduction was always observed) and

forward (where for c close to the near-wall turbulence convection velocity, a drag increase was observed).

The parameters at which drag reduction, %DR, by spanwise oscillations occurs have been investigated thoroughly. In Quadrio and Ricco (2004)'s DNS, the period of oscillation T and spanwise maximum velocity W_m were varied and the %DR and net energy saving, $P_{sav,net}$, were reported for each case. For an actuator vibrating at fixed T, %DR increased with increasing oscillation amplitude D_m. The optimum non-dimensional oscillation period, $T^+ = \frac{T u_\tau^2}{\nu} = 100 - 125$, enabled positive $P_{sav,net}$ for low to moderate D_m.

Ricco and Wu (2004) studied the Re-dependence of the drag reduction through experiments at $\mathrm{Re}_\theta = 500, 950$ and 1400 finding no significant differences for constant T^+ and $D_m^+ = \frac{D_m u_\tau}{\nu}$. In contrast, Il-Choi et al (2002)'s DNS showed strong Re-dependence, revealing this as an unresolved issue.

Previous experimental studies of this technique employed crank-driven flat plates where T or W_m could be altered by changing the crank-speed but D_m was fixed. The crank mechanism is ideal for low W_m experiments but does not lend itself to deployment to an engineering application for end use. In this experiment two resonant surfaces based on the well-established principle of the linear induction motor and on the novel field of EAPs in DEA mode, were developed. Both designs are based on a flat plate driven at resonance as governed by the stiffness of restoring springs and the mass of the oscillating parts. Whereas the linear induction motor version has the advantage of being a stand-alone tile requiring only two current-carrying conductors to the motor coil, the EAP version has a further advantage of being a stand-alone tile where the restoring springs and the prime mover are one and the same element.

The remainder of this paper is organised as follows. Section 2 describes the experimental design and setup. Section 3 describes the actuators design including a description of EAPs followed by section 4 where results from the three measurement systems are presented .

2 General Setup & Design of Experiment

The wind tunnel used in all experiments is open circuit with a test-section cross-sectional area of 0.76 m × 0.76 m and a 3 m fetch. Air is driven by a centrifugal fan and the tunnel has a contraction area ratio of 4.6, a series of wire-meshes and a honeycomb for flow conditioning. The free-stream turbulence intensity of the tunnel, based on the streamwise fluctuation velocity is about 0.5%. The ceiling was adjusted to obtain a zero streamwise pressure gradient as monitored by a series

of pressure taps along the streamwise coordinate of the plate. The tunnel speed was maintained uniform using a closed loop PID controller implemented in NI Labview using a Furness FCO510 micro-manometer equipped with thermocouple and atmospheric pressure sensor for velocity updates in response to changes in freestream temperature and atmospheric pressure. Measurements were made on a flat plate, mounted at the tunnel half-height with a super-elliptical leading edge and a tapered trailing edge with a small control surface for fine adjustments of the pressure gradient and circulation. The boundary layer was tripped. Approximately 2.4 metres downstream of the leading edge, the flat-plate housed an air-bearing, a major component of the drag balance, as shown in figure 1.
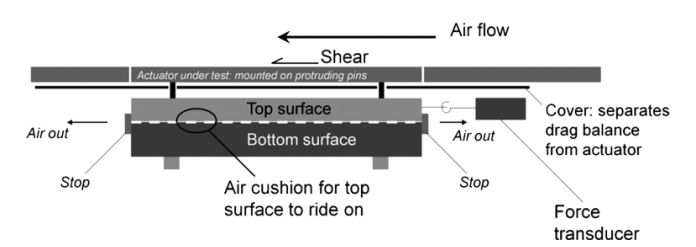
Fig. 1 A schematic of the actuator mounted on top of the drag balance.

The air-bearing, of dimensions 30 cm × 30 cm, figure 2 was mounted on three screws for height adjustment and accurate levelling. The actuator sat on four pins screwed into the bearing's floating element and a plate separated the air-bearing from the actuator, preventing contamination of the boundary layer by the lifting air, figure 1.

For each of the experiments, a zero pressure gradient was established and hence the static pressure differential across the drag balance was negligible. An isometric force transducer from Hugo Sachs Elektronik - Harvard Apparatus GmbH, model F10, was used for direct friction-drag measurements. Its range is ±10 grams over a displacement range of ±60 μm and is set up as a full ohmic bridge with nominal resistance of 1 kΩ driven by a Fylde bridge amplifier. The air-bearing-force-transducer system was levelled and set up carrying a 30 cm × 30 cm actuator-carrying tray leaving a 0.5 mm gap all around, and the tray edges were flush with the surrounding surface. Given the mass of the floating element of the drag balance, its frequency response was found to be less than 3 Hz.

The measured values of friction drag were shown to be close to what was theoretically predicted, and a measure of sensitivity was obtained through an exercise
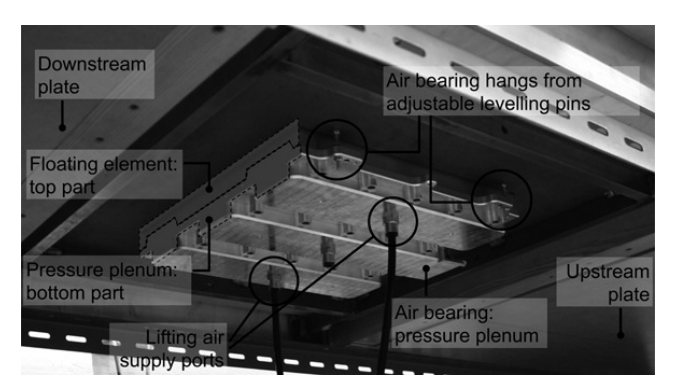

Fig. 2 A view of the air-bearing from the bottom. The air-bearing is shown hanging from screws for bearing-levelling. The cross-sections of the top (floating element) and bottom (pressure plenum) parts are shown shaded. Also shown are the lifting air supply ports and parts of the plates upstream and downstream of this middle portion.

where, using the tunnel PID controller, the freestream velocity was adjusted to the value at which the experiments were to be conducted. Small percentage changes were then imparted to the freestream velocity which, after a period allowing for stabilisation, was measured together with the friction drag. Figure 3 shows the results from one of these trials plotted against the force predicted from an analysis in boundary layer growth in Schlichting (1968).
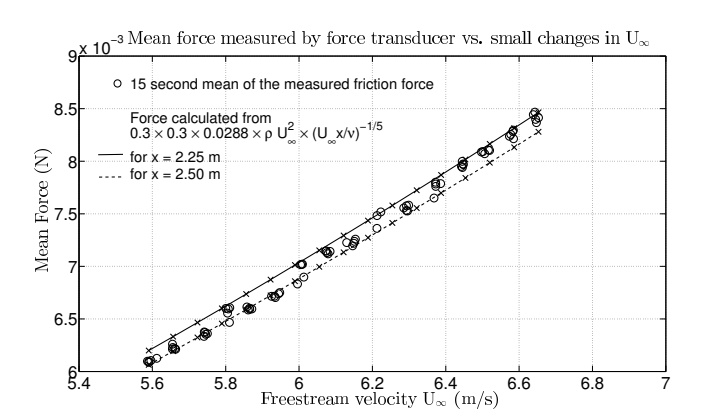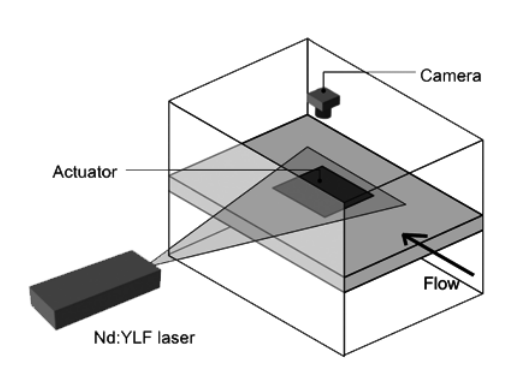

Fig. 3 A plot of the variation in measured friction drag *vs.* small changes in the freestream velocity. The data is compared with a theoretical expression from an analysis in boundary layer growth in Schlichting (1968).

A constant-temperature anemometer (CTA) model DISA 55M10 was used in conjunction with a single, miniature, hot wire probe. An overheat ratio of 1.5 was selected. This lower value was selected to minimise the heat loss to the actuator surface and hence the influ-

ence that this might have on the velocity measurements. Data from the anemometer were DC-shifted, amplified and low-pass filtered prior to acquisition by an NI-6259 DAQ card. The hot-wire was calibrated in the wind-tunnel against a Pitot-static probe, before and after the experiment, and an interpolation in time was utilised in the conversion of data. The data set was discarded if the temperature change between the two calibrations was in excess of 1.5 °C. The hot-wire was moved inside the wind-tunnel using a motorised traverse with a resolution of 2.5 μm and an accuracy of ± 2.5 μm.

A time-resolved PIV system from Dantec Dynamics was also set up, figure 4. The beam, approximately 0.5 mm thick, or 8 wall units, (although its intensity distribution is Gaussian), was parallel to the actuator plane and set such that its mid-plane was at a height equivalent to $y^+ \approx 15$. Given the beam thickness compared to the linear sublayer thickness and the high shear associated with the region, a degree of spatial averaging is inevitable. The seeding particles, olive oil droplets of diameter ≈ 3 μm, were generated using a Dantec Dynamics Liquid seeding generator model 10F02.
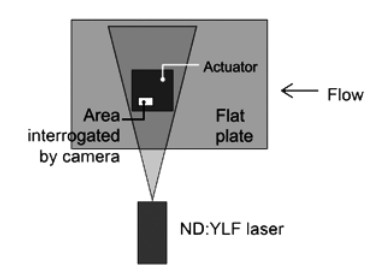

Fig. 4 The general setup of the PIV system showing the position of the laser beam and the camera in relation to the actuator.

2.1 Experiment Design

The simulations of Quadrio and Ricco (2004) that had shown close agreement with earlier experimental work were chosen as the basis for the design of the present experiment. Since in this experiment, $\mathrm{Re}_\theta = \frac{U_\infty \theta}{\nu} \approx 2500$, ($\theta$ is the momentum thickness) is approximately twice the highest Reynolds number reported in literature, an initial assumption that the non-dimensional quantities indicated for drag reduction in Quadrio and Ricco (2004), still scale at this higher Re. u_τ as obtained from a turbulent boundary layer growth theoretical model in conjunction with the drag-reduction map from Quadrio and Ricco (2004) were used to obtain the necessary dimensional quantities for the current experiment as shown in Table 1 and in figure 5.

	Non-Dimensional	Dimensional
U_∞		6.25 m/s
u_τ		0.25 m/s
Period	$T^+ = \frac{T u_\tau^2}{\nu} = 100$	0.024 s
Frequency (T^+=100)	$f^+ = \frac{f \nu}{u_\tau^2} = 0.01$	42 Hz
wall unit ν/u_τ	1	60 μm
linear sublayer height	5 wall units	300 μm
amplitude of oscillation	$D_m^+ = \frac{D_m u_\tau}{\nu} = 66, 100, 133$	4, 6, 8 mm
Stokes layer depth of penetration)	14 wall units	800 μm

Table 1 The theoretical conditions on which the current experiment was designed.

3 Actuator

The two tile actuators developed here are both resonant devices executing in-plane spanwise oscillations with amplitude close to, or larger than the turbulent flow mean streak spacing. No energy consumption measurements were made here but the authors believe that a resonant design is the most promising if a net energy saving is to be attained in an aerodynamic drag-reduction application. Both surfaces are based on a rigid 30 cm × 30 cm outer frame which maintains its
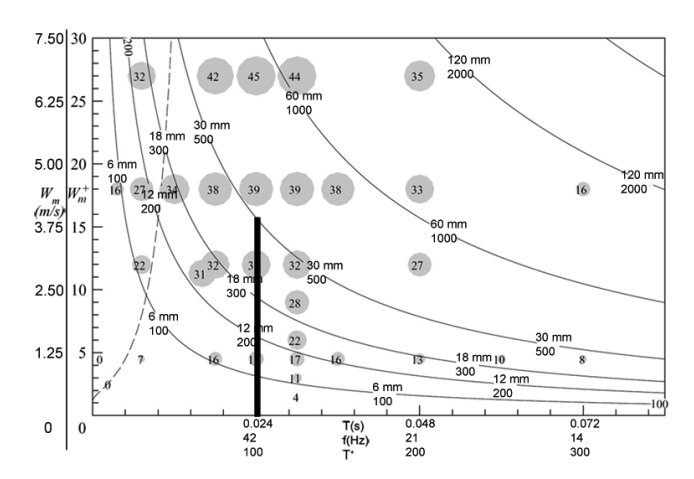
Fig. 5 The map of Quadrio and Ricco (2004) converted to the conditions of the current experiment. The current actuator designs maintain the same frequency but the amplitude of oscillation can be varied, hence climbing along the vertical bold line shown.

dimensions and an inner, smaller, rectangular frame designed to oscillate at its fundamental frequency, $f \approx 42$ Hz (or equivalent period, $T^+ \approx 100$), as governed by the mass of the oscillating inner rectangular frame and the stiffness of the restoring springs. In the case of the electromagnetic driven surface, activation was achieved through the linear motor principle. In the EAP version of the surface, the actuator and the restoring springs are one and the same electrically-tuned polymer. Both actuators are fully described by Gouder (2011).

3.1 Electroactive Polymer (EAP) Actuator

The principle of operation of an EAP actuator (in DEA mode) is shown in figure 6. An elastomeric film – the dielectric medium – is sandwiched between two electrically conductive, compliant electrodes, Pelrine et al (1997). This is, in principle, a compliant capacitor, made from an incompressible and highly deformable elastomer with compliant electrodes that do not stiffen the dielectric medium, Kofod (2001).

Applying a voltage difference between the electrodes, Coulomb electrostatic forces are created which cause a contraction of the actuator along the electric field direction and an expansion of it along the two orthogonal directions, Pelrine et al (1997). The compressive stress acting in the thickness direction is given by:

$$p = \epsilon\epsilon_0 E^2 = \epsilon\epsilon_0 \frac{V^2}{z^2} \tag{1}$$

where, E is the electric field (Volts per metre) given by $\frac{V}{z}$ where V is the applied voltage and z is the thick-
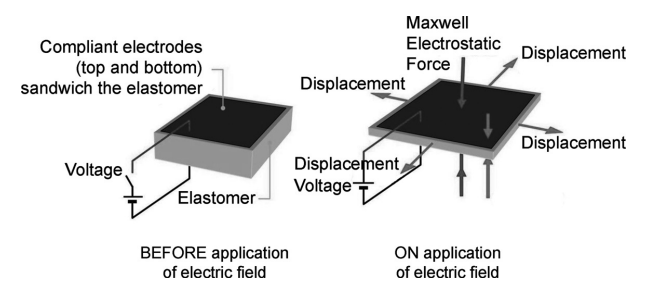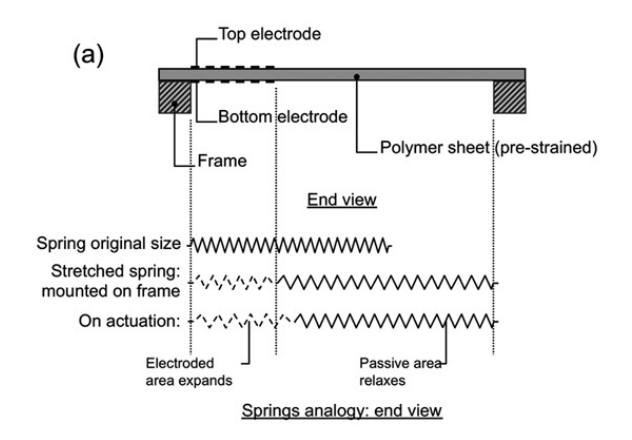

Fig. 6 Principle of operation of a DEA.

ness of dielectric elastomer. ϵ is the elastomer's dielectric constant (≈ 2.8 for silicones) and ϵ_0 is the permittivity of free space (8.85×10^{-12}F/m). DEAs have been demonstrated to produce large strains, fast response times, $\mathcal{O}(\mu s)$, and high electromechanical efficiency ($>90\%$). Such promising performance has been exploited and has led to numerous tentative applications including artificial muscles for robots, linear actuators, refreshable Braille systems and flow-control devices such as dimples, Dearing et al (2007) and Dearing et al (2010). These actuators, however, require high voltages to operate, $\mathcal{O}(3)$ kV, and the technology is still immature, often leading to fragile actuators with a high proportion of high-voltage burn-through failures.

The in-plane prime-mover / driver part of the actuator was designed by developing the EAP principle of figure 6, introducing pre-strain in the elastomer. Referring to figure 7(a), a polymer membrane is stretched in its plane, transferred to a holding frame in its strained state and electrodes patterned on both its surfaces. On actuation, the elastomer portion between the electrodes (here called active) is compressed in thickness and hence expands in area but since the membrane is pre-strained, while the active portion elongates, the passive portion relaxes. If the actuation strain is smaller than pre-strain, all deflections occur in the sheet's plane without any buckling which would cause out-of-plane movement. The actuator consists of two parts: a) the EAP driver described and b) a passive sheet, driven by the EAP driver and exposed to the air flow in the wind-tunnel. The EAP driver and the passive sheet are connected by an I-shaped member that extracts the maximum amplitude of movement of the former and transfers it to the driven sheet. The principle of operation of this actuator is explained in figure 8.

The two electrode pairs are driven in anti-phase with an arbitrary waveform resembling a DC-shifted sine wave as programmed in a bespoke LabView program, supplied by two NI-6259 DAQ analogue outputs and amplified by two TREK High-Voltage Amplifiers model 609E-6. When driven at the resonant frequency
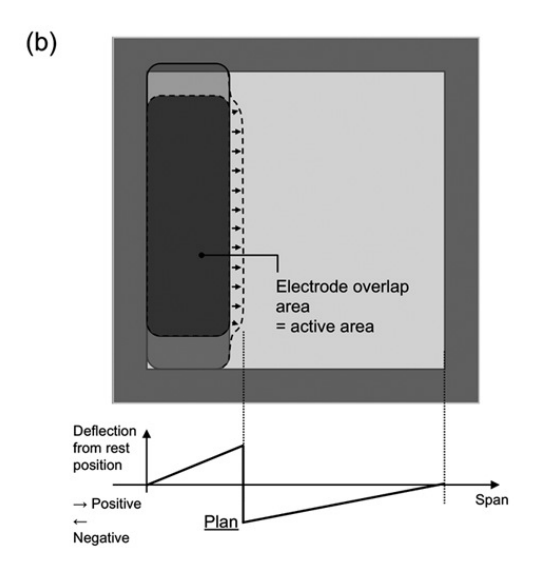
Fig. 7 *a)* An end view of a typical pre-strained actuator and a springs analogy. *b)* A plan view of a typical pre-strained actuator during actuation showing the displacement of the active and passive areas relative to their unactuated position.

(as governed by the elasticity of the EAP driver membrane and the mass (primarily) of the I-section) large oscillations of the driven sheet occur.

3.1.1 In-plane actuator: Design and fabrication details

A 250 μm thick sheet of Nusil MED-4905 silicone elastomer with initial dimensions of 18.3 cm × 10.3 cm was stretched to 25.4 cm × 25.4 cm, i.e. the external size of a glass-fibre composite frame which was then carried by a 30 cm × 30 cm tray tile. This gave membrane pre-strain values of 250% and 67%. This unequal biaxial pre-strain produced an anisotropy in the membrane, specifically, a smaller Young's modulus in the lower pre-strain direction. This caused the thickness change introduced by the electrostatic forces to be transformed mainly in an in-plane strain in the low-modulus direction, which,
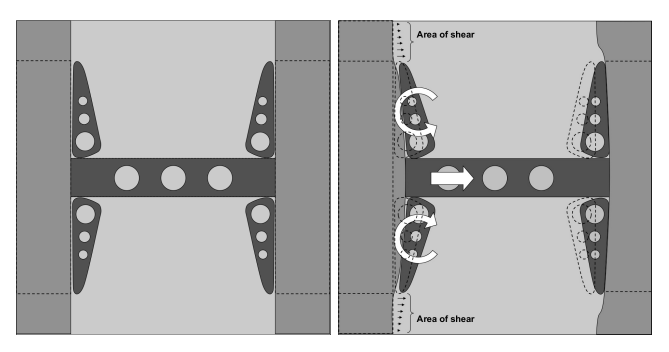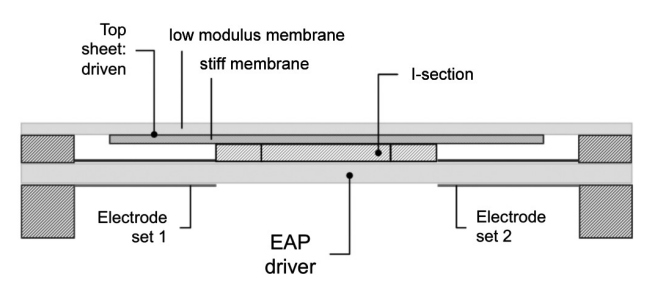

Fig. 8 *Left:* A schematic of the I-section glued onto the pre-strained membrane. The electrodes (both OFF) are shown as strips either side of the frame and the active area lies within the dashed rectangles. *Right:* The actuator with the left electrode made ON. The side arms of the I-section are tapered and separate from the middle member to reduce the effect of resistive shear stresses from the side portions of the frame. The position of the electrode and side arms of the I-section prior to actuation are shown in dashed lines.

Fig. 9 A schematic of the assembled actuator featuring the EAP prime mover, I-section and the driven sheet consisting of a stiff membrane-low modulus membrane sandwich. The stiff membrane distributes the movement of the I-section over a large area while the low-modulus sheet on the perimeter allows in-plane movement and seals the periphery.

aligned transversally to the air flow direction, made it the desired actuation direction. A bespoke numerical simulation, Potter et al (2011), was developed to predict and optimise actuator performance.

Conductograph GFG5 graphite electrodes 3 cm wide with an overlap length of 20 cm were brushed onto the membrane. Obvious imperfections (trapped air bubbles and scratches with a density of one defect every 2.5 cm^2 of membrane are common) in the pre-strained membrane were not covered by the electrodes. Such defects are sites of premature membrane failure mainly through a short circuit between electrodes due to the reduced local breakdown voltage. The electrodes were connected to the high-voltage TREK amplifiers through

aluminium foil leads. The final form of the I-section with holes to adjust its mass and hence the actuator's resonant frequency, around 42 Hz equivalent to $T^+ \approx 100$, is shown in figures 8 and 9.

3.2 Electromagnetic Actuator

The electromagnetic actuator developed here is based on a flat plate of known mass suspended between four springs of equal stiffness, driven at resonant frequency, around 44 Hz, figure 12, by a miniature linear-induction motor developed in-house. A bespoke circuit based on a push-pull transistor pair was developed to drive the coil of the electromagnetic linear motor. A set of sliding bearings were installed to limit unwanted motions in directions other than the spanwise.
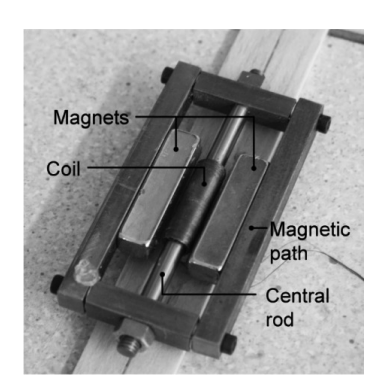

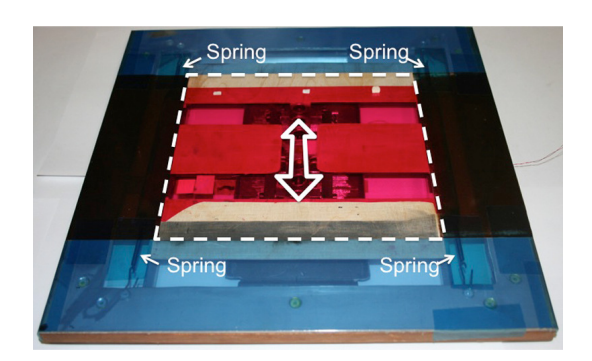**Fig. 10** The electromagnetic linear motor showing the magnetic path, the central rod, the magnets and the coil.

Fig. 11 The electromagnetic linear-motor-driven actuator. The area enclosed in dashed lines is the oscillating portion.
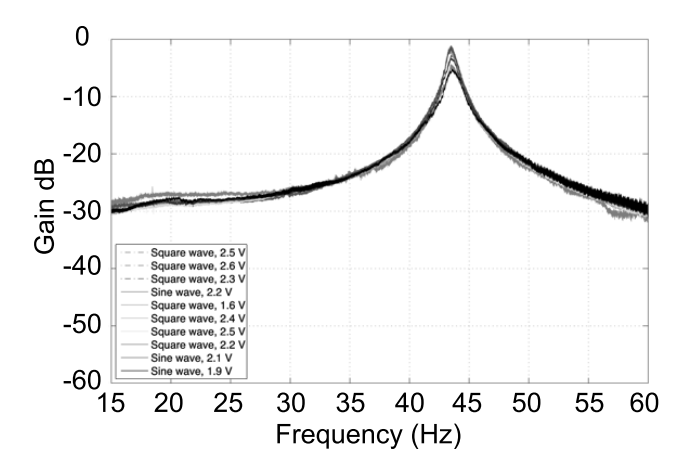

Fig. 12 The Bode plot for magnitude for the electromagnetic actuator obtained through a chirp signal through a frequency range including resonance.

4 Results

4.1 Hot-wire measurements

A number of hot-wire traverses were conducted over both oscillating surfaces. Figure 13 shows mean velocity profiles from traverses over the EAP surface, normalised by u_τ of the unactuated case. Ignoring data lower than $y^+ \approx 2.5$ due to suspected increased hot-wire heat loss to the wall, the wall-normal mean-velocity gradient is observed to decrease for actuated cases indicating a drag reduction.
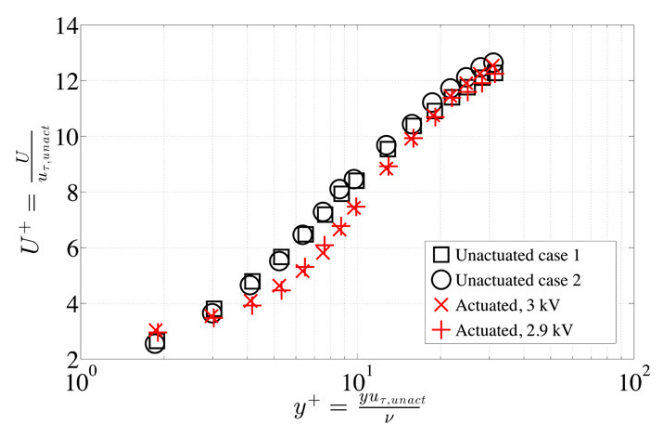

Fig. 13 Mean streamwise velocity profiles at a streamwise location close to the trailing edge of the EAP spanwise oscillating wall scaled with friction velocity of the uncontrolled case. The curving up of the actuated case profile at low values of y^+ is attributed to higher heat transfer to the wall; data below $y^+ < 2.5$ were considered contaminated by this excess heat transfer.

A more elaborate set of measurements was obtained over the electromagnetic actuator surface, owing to its higher robustness and reliability. Table 2 is a summary of the relevant parameters.

U_∞	δ	δ_1	θ	C_f	Re_θ	u_τ	Re_τ
m/s	mm	mm	mm			m/s	
6.25	54	8.03	5.91	0.00312	2430	0.248	900

Table 2 Table showing the relevant parameters that describe typical base flows investigated where:
displacement thickness = $\delta_1 = \int_{y=0}^{\infty}(1 - \frac{U}{U_\infty})\mathrm{d}y$,
momentum thickness = $\theta = \int_{y=0}^{\infty}\frac{U}{U_\infty}(1 - \frac{U}{U_\infty})\mathrm{d}y$.

The Stokes Reynolds number, $Re_{\delta,sl} = U_0\delta_{sl}/\nu$ ($\delta_{sl} = \sqrt{2\nu/\omega}$, and ω is the flat plate oscillation frequency) was kept well below the lowest critical value reported in literature, i.e. $Re_{\delta,sl} = 142$ (Kamphuis (1975)) in all experiments, following studies by Akhavan et al (1991a) on the Stokes layer's transition to turbulence.
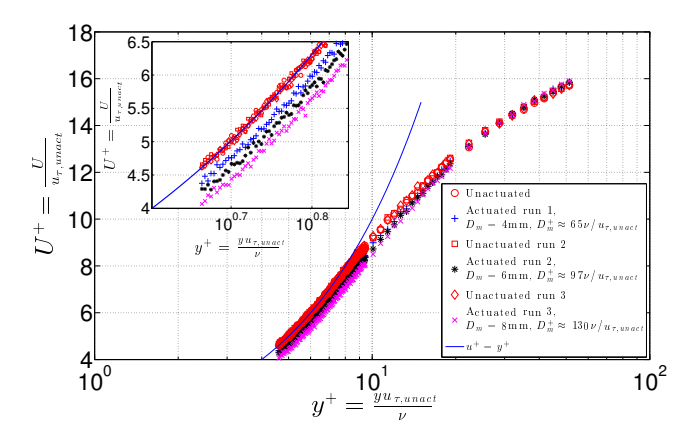

Fig. 14 Non-dimensional mean velocity profiles of the six tested cases obtained approximately 1.5 cm from the trailing edge of the electromagnetically-driven oscillating surface; data were normalised by the estimated friction velocity from the unactuated cases, $u_{\tau,unact}$.

Figure 14 shows six mean velocity profiles obtained close to the trailing edge of the electromagnetic actuator surface, normalised by the estimated friction velocity from unactuated cases, $u_{\tau,unact} = 0.248$ m/s. The data have been corrected for yaw effects due to the Stokes layer spanwise velocity by i) assuming a yaw coefficient for the hot-wire and ii) reconstructing the Stokes layer velocity by simultaneously recording the oscillating wall position (through a laser profilometer) and the hot-wire signal; corrections were, however, neg-

ligible. Data affected by heat transfer due to surface proximity were truncated using a Diagnostic Plot presented by Alfredsson et al (2009). The electromagnetic actuator oscillated at 42 Hz equivalent to $T^+ \approx 90$ and data for cases where $D_m = 4$, 6 and 8 mm were recorded. Figure 15 shows the same data normalised by the estimated friction velocity from each of the individual actuated cases, $u_{\tau,act} = 0.242$ m/s for the $D_m = 4$ mm case, 0.238 m/s for the $D_m = 6$ mm case and 0.234 m/s for the $D_m = 8$ mm case. A small correction was applied to the y coordinates of the set until a linear regression best fit through the unactuated cases data between $y^+ = 3.5$ and 6. It is observed that when the data are normalised by $u_{\tau,unact}$, the profiles for actuation fall below the relationship $y^+ = u^+$ onto which the unactuated case collapses (see inset plot, figure 14), indicating a drag reduction. It is also observed that at the start of the log region, data for drag reduction cases shift slightly above those for the unactuated case to maintain flow continuity. On the other hand, using $u_{\tau,act}$ to normalise each data set independently, causes the data for all cases to collapse in the sublayer (see inset plot, figure 15). The data in the log region are shifted upwards as the drag reduction increases. It was also observed that the region in which $u^+ = y^+$ is extended for cases of drag reduction, indicating a thickening of the linear sublayer.
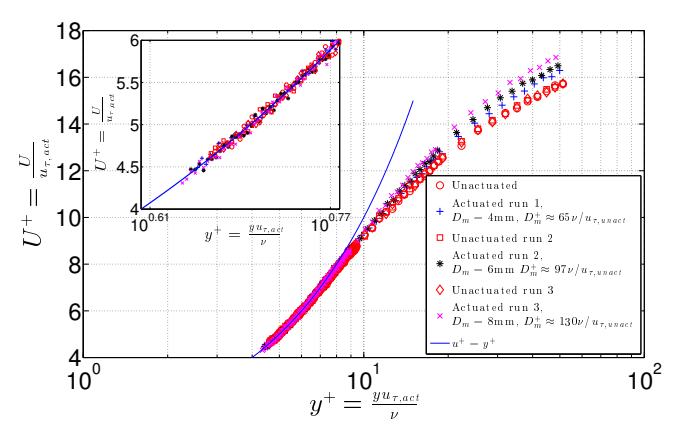

Fig. 15 Non-dimensional velocity profiles from figure 14 normalised by the estimated friction velocity from each of the individual actuated cases, $u_{\tau,act}$, showing collapse close to the wall and an outward shift for actuated cases.

The mean-square fluctuation of the streamwise velocity is shown in figure 17 where $\overline{u^2}$ is normalised by $u^2_{\tau,unact}$. Data from Fernholz et al (1995) has been included for comparison; in the current work, the non-dimensional probe size $l^+ \approx 16$ was approximately twice Fernholz et al (1995)'s and the freestream turbulence
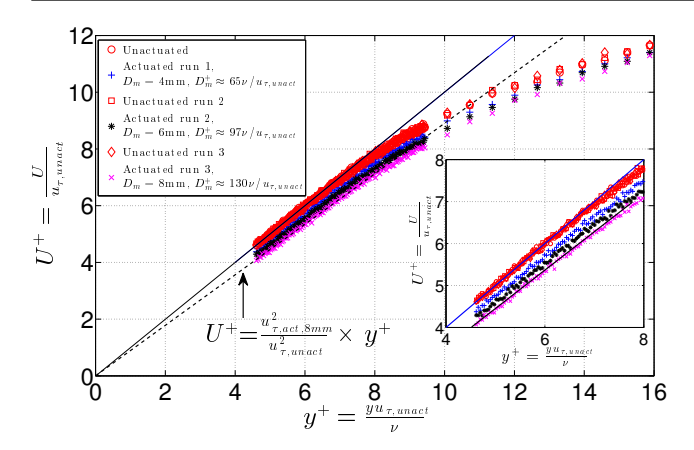
Fig. 16 Non-dimensional plot of the data from figure 14 on linear axes (as opposed to log x-axes) showing the shallower gradient of actuated cases.

Fig. 18 Non-dimensional plot of the mean-square fluctuation streamwise velocity non-dimensionalised by the estimated friction velocity from the individual cases.
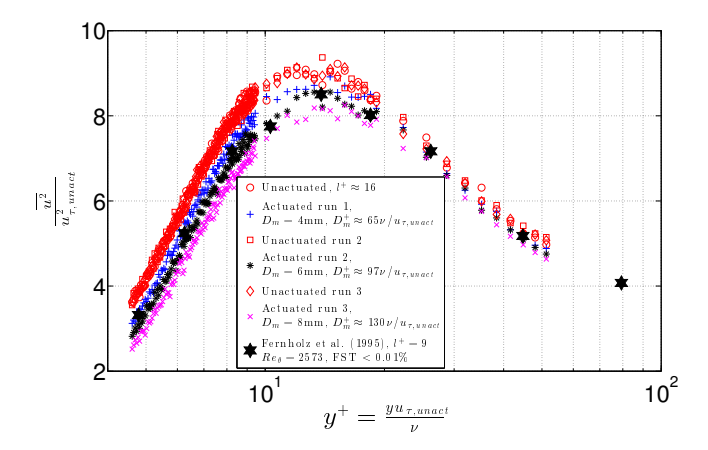

Fig. 17 Non-dimensional plot of the mean-square fluctuation streamwise velocity non-dimensionalised by the estimated friction velocity from the unactuated cases, $u_{\tau,unact}$. Data from Fernholz et al (1995) for the conditions shown in the figure's legend are also included for comparison.

intensity (FST) was approximately 0.5%, explaining the slightly higher mean square values reported here compared with literature. Referring to figure 17, it is seen that for the unactuated case, the peak is approximately at $y^+ = 15$ whereas for the actuated cases, reductions of approximately 12% in $\overline{u^2}$ are observed for the $D_m = 8$ mm case, and their peak moves above $y^+ = 15$ with increasing D_m, confirming the thickening of the linear sublayer. As with the mean velocity profiles, $\overline{u^2}$ data were also normalised by the individual value of u_τ, figure 18. It is observed that the profiles now collapse in the viscous sublayer but, in the linear sublayer (below $y^+ \approx 7$), the profiles for cases of drag reduction fall slightly below the unactuated data (see inset). The lack of complete collapse of profiles indicates that
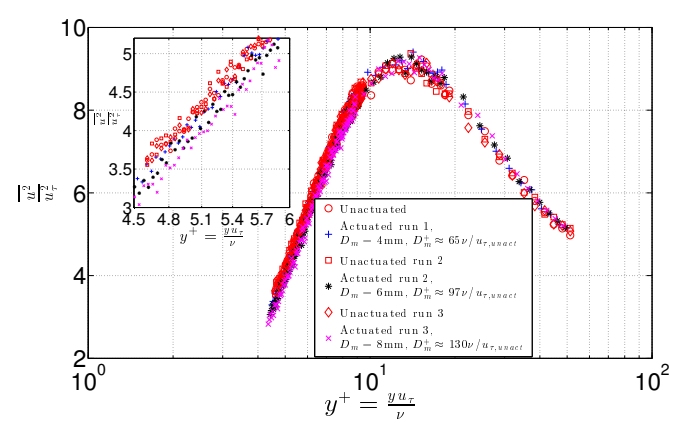
the change due to actuation involved more than just a diminution of the wall-normal gradient (as indicated by the reduction in the friction velocity); a more fundamental change in the near-wall turbulence structure and its feedback mechanisms is revealed (Ricco, P., personal communication).

An increase in skewness was also observed, figure 19 (top). Although the skewness peak was not captured, the trends suggest that this peak moves away from the wall and that the skewness has also been made positive at wall-normal locations where previously it had had a negative value. An increase in kurtosis was also observed. Both these increases were investigated by plotting the pre-multiplied probability distribution functions [pdfs] (not shown). It was observed that contributions to the increase in skewness and kurtosis come from both the reduction in the small negative side of the pdf and also from the enhancement of intermittent large positive events (enhancement of some high-speed streaks), bringing a clarification to the disagreement between results interpretation by Il-Choi et al (2002) and Choi and Clayton (2001).

In order to capture the spatial transient, measurements were performed at various streamwise locations. Figure 20 shows a plot of %DR as estimated by the reduction of the wall-normal gradient, against the streamwise distance from the leading edge of the oscillating surface. A *local* maximum of 11.5% was attained close to the oscillating plate's trailing edge for the $D_m = 8$ mm case. Larger drag reductions of up to approximately 16% were attained for wall peak-peak amplitudes of approximately 10 mm ($\approx 164 \ \nu/u_\tau$). However owing to actuator failure, the data were not of sufficient quality (length of acquisition and number of data points in the linear sublayer) to determine the drag reduction with
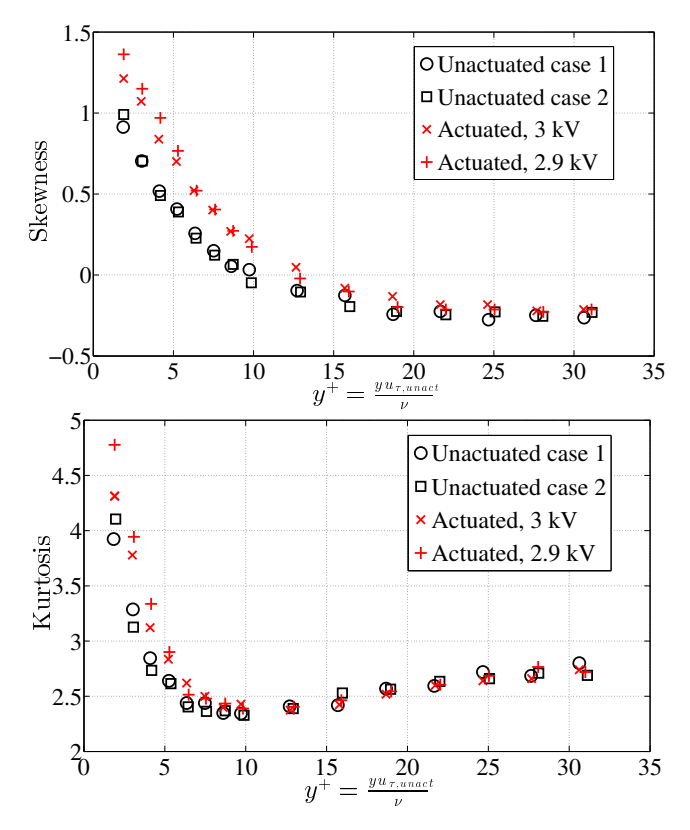
Fig. 19 (*top*) Skewness, (*bottom*) Kurtosis, of the streamwise velocity fluctuating component in the turbulent boundary layer, with control and without control, obtained over an EAP surface. The voltage values in the legend refer to the EAP actuator driving voltage and correspond to $D_m \approx 4$ mm.

sufficient certainty. In the same figure, drag-reduction values from equivalent runs of the DNS reported in Quadrio and Ricco (2004), $\mathrm{Re}_\tau = 200$, kindly run by Professor Maurizio Quadrio specifically for comparison with the current work, are included. The drag reduction values from the DNS are a few percentage points higher than the present experimental values. For the $D_m = 6$ mm and more so, for the 8 mm case, data in Quadrio and Ricco (2004) indicate the present oscillating surface was not quite long enough to attain a drag reduction value beyond the spatial streamwise transient. This is supported by the trends for the $D_m = 6$ and 8 mm in figure 20 which indicate a-still increasing level of drag reduction with streamwise distance at the plate's trailing edge.

The spatial transient had consequences for the integrated drag, as would later be measured for example by a drag-balance, because this would measure the *total* drag on the surface, hence integrating the effect of the spatial transient. The integrated value is therefore substantially lower than the local maximum attained here,

as discussed next and in the following section. The actuator tile had a footprint of 30 cm × 30 cm mounted on a drag balance of equal proportions; however due to the tile's design, only a portion of dimensions 16 cm in the streamwise × 20 cm in the spanwise direction (oscillating area : total tile area = 3.2 : 9) could be made to oscillate. This led to a further decrease in the integrated drag reduction over the tile because areas upstream, downstream and adjacent to the oscillating surface had small or no drag reduction, but were still carried by the drag balance. The three dashed horizontal lines towards the lower part of figure 20, annotated $D_m = 8$ mm etc., represent the drag reductions obtained by integrating under the three drag reduction curves in the same figure (between the oscillating plate's leading and trailing edges), and multiplying by the area ratio 3.2 : 9, and expected to be close to what a drag balance would then read.
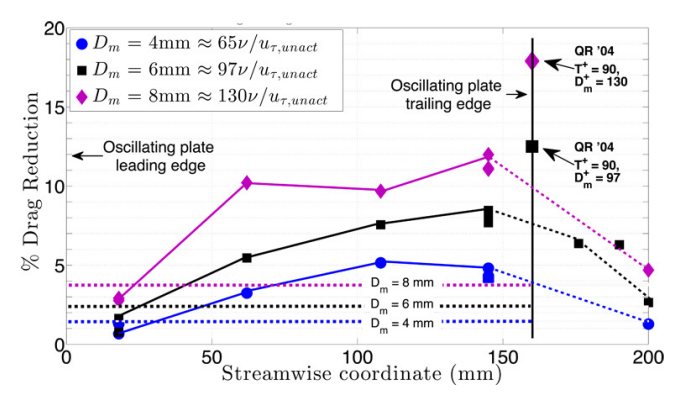

Fig. 20 A plot of %DR estimated from wall-normal hot-wire traverses at various streamwise coordinates relative to the leading edge of the oscillating plate for the three oscillation amplitudes. The three horizontal dotted lines indicate the *integrated* drag reduction for each case, multiplied by the factor 3.2:9, which is the area ratio of the oscillating portion to the total portion, particular to this experiment. The integrated drag value was obtained by integrating underneath each of the transient curves in the figure between the plate leading and trailing edges and dividing by the plate length. Also shown are the %DR values from Quadrio and Ricco (2004)'s DNS, annotated as QR'04. (The data points have only been joined for clarity.).

4.2 Direct Drag Measurements

When direct drag measurements were attempted using the EAP actuator, rogue electrostatic forces were generated by the high-voltage supply leads and electrodes;

measures taken to remove them, detailed in Gouder (2011), proved ineffective. It was discovered that, in all cases where rogue forces were observed, the high-voltage waveform had a non-zero time-mean. The two waveforms – in anti-phase to one another – used to power the two electrodes of the EAP actuator described in 3.1, did not have a zero time-mean in order to cause a time overlap between them and hence harness the oscillating plate inertia to get larger deflections. Direct drag measurements for an EAP actuator were, hence, not performed.

On the other hand, direct drag measurements were performed on the electromagnetic actuator surface. Following a period of drag measurement with the actuator switched off, the actuator was then switched on for a period of, typically, 60 seconds. Measured batches of friction-drag force, $\mathcal{O}(1)$ gram, fifteen seconds long were averaged and plotted against time. When the actuator was switched off, checks were made to ensure that the reading returned to its unactuated value. Figure 21 shows two time-series of drag measurements showing drag reductions for the $D_m = 8$ mm case. The measured drag reductions were smaller than 2% and hence slightly larger than data scatter. This is also approximately half of the *integrated* drag reduction (accounting for oscillating : total area as well) shown in figure 20 for similar conditions. The version of the electromagnetic actuator surface tested during direct measurements, with its constraint to be as light as possible to minimise its destabilising effect on the drag balance, had limited rigidity and surface flatness, causing slight deformations (as seen through a high-speed camera), which, the authors deem to have affected the direct drag measurements through the introduction of time-dependent surface roughness.
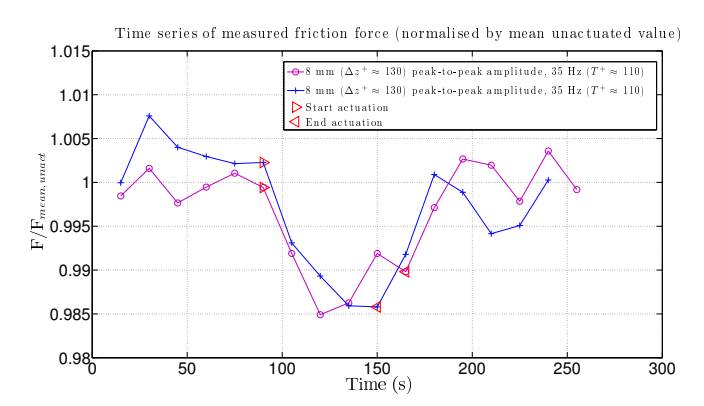
4.3 PIV measurements

The PIV system was set up as described in section 2 and in figure 4. Figure 22 shows the mean-square distribution of the streamwise fluctuating component for the unactuated case, the $D_m = 6$ mm ($D_m^+ = 97\nu/u_\tau$) case and the $D_m = 8$ mm ($D_m^+ = 130\nu/u_\tau$). The reduction for the 8 mm case is approximately 14% in close agreement with hot-wire data obtained at the same streamwise location. Each image was obtained from a total of eight data-sets, each of 4108 images acquired at a rate of 700 image-pairs/s with a laser pulse separation of 140 μs. The images were pre-processed to remove stray reflections by subtracting the minimum of each batch of 4108 images. The mean that was subtracted from the total velocity to obtain the mean-square of the fluctuating component distributions is an ensemble average of the eight data sets. A 4 step iterative window-offset cross-correlation analysis was performed using 32x16 pixel interrogation areas and 50% overlap. Between each algorithm pass, a validation based on a local 5x3 median filter and correlation peak height (p_1/p_2) was used to reject anomalous vectors. The distributions in figure 22 have attained temporal convergence but still exhibit slight variations due to small spatial surface gradients.

The local spanwise velocity values for each image were averaged and plotted against time as shown in figure 23. For cases of no actuation, no particular time-dependent behaviour is noted but rather a more broadband plot as expected. For actuation cases, however, a sinusoidal behaviour is observed at the frequency of actuation indicating a surface modulation of streak structures.

5 Conclusions

In this work, a study of turbulent boundary layer control by means of a spanwise oscillating surface has been pursued. The parameters that governed the required performance of the oscillating surface for drag reduction were based on DNS reported in literature, mainly the work by Quadrio and Ricco (2004). Two technologies were pursued in building the oscillating surface: i) Electroactive Polymer (EAP) in the Dielectric Actuator mode and ii) Electromagnetic actuators. Hot-wire measurements, PIV measurements and direct drag measurements were carried out on the oscillating surface mounted in the wind-tunnel. The two actuators are original in design and significant contributions have been made to the field of EAPs. From hot-wire measurements on the actuator, a maximum drag reduction
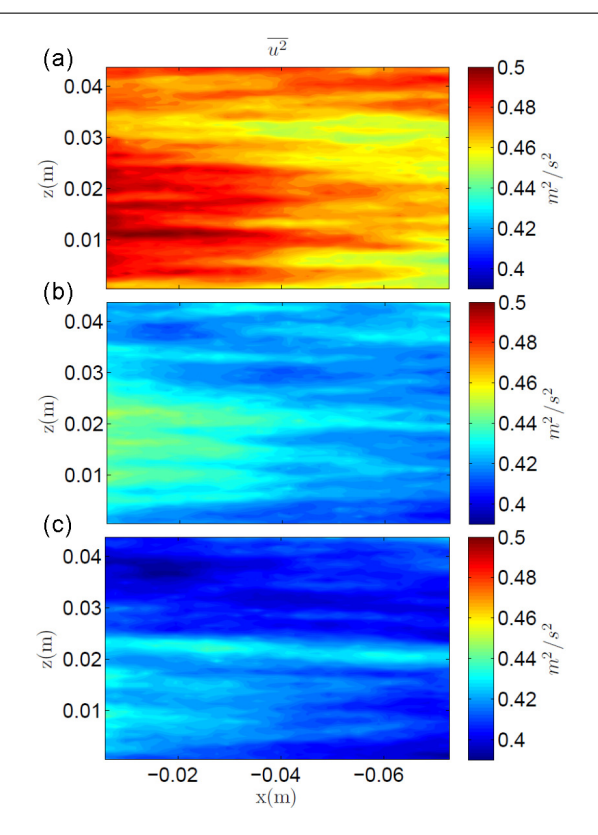

Fig. 21 Direct drag measurements showing a reduction in drag for actuation. In these cases $T^+ \approx 110$. Two runs are shown.

Fig. 22 The mean-square distribution of the streamwise fluctuating component $\overline{u^2}$ for (a) the unactuated case, (b) with $\Delta z = 6$ mm ($\Delta z^+ = 97\nu/u_\tau$) and (c) with $\Delta z = 8$ mm ($\Delta z^+ = 130\nu/u_\tau$). The interrogation frame was close to the actuator's trailing edge as shown in figure 4.
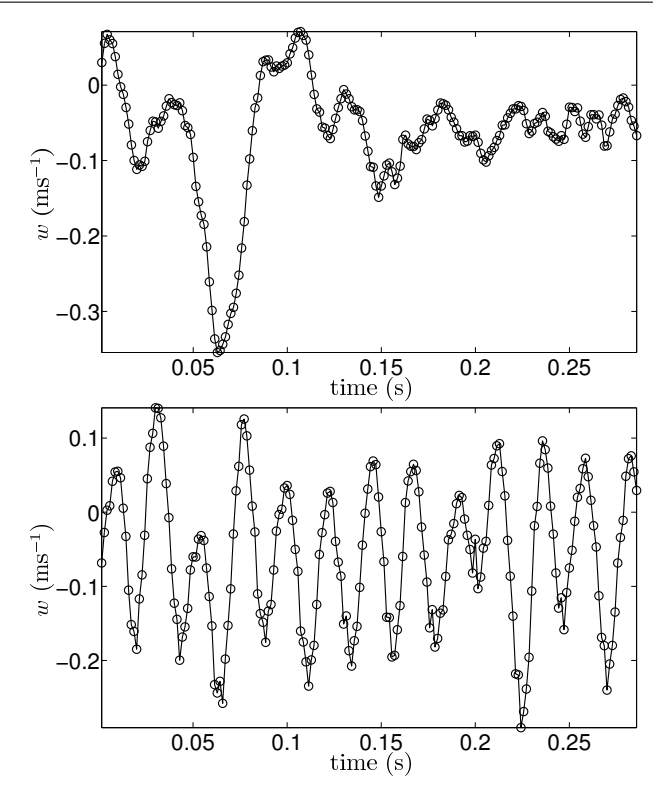

Fig. 23 The mean spanwise velocity of the flow at the laser plane as a function of time: (*top*) for no actuation; (*bottom*) for $\Delta z = 8$ mm ($\Delta z^+ = 130\nu/u_\tau$), revealing a dominant frequency equal to the actuation frequency, showing how the actuator motion modulates the streaks.

of 11.5% was measured for oscillation conditions of 43.9 Hz ($T^+ \approx 90$) and a peak-to-peak amplitude of 8 mm equivalent to approximately 130 ν/u_τ. This, and other drag measurements were slightly lower than what has been reported in literature reporting DNS and lower Reynolds number experiments. Larger drag reductions of up to approximately 16% were attained for wall peak-peak amplitudes of approximately 10 mm ($\approx 164\ \nu/u_\tau$). However owing to actuator failure, the data were not of sufficient quality (length of acquisition and number of data points in the linear sublayer) to determine the drag reduction with absolute certainty. The *integrated* drag reduction measured from the drag balance was about 1.5% owing to a) the streamwise spatial transient starting from the leading edge (where no drag reduction is expected) of the oscillating portion (the 11.5% dreg reduction reported was measured close to the trailing edge of the oscillating plate), and b) the fact that of the 30 cm × 30 cm actuator surface mounted onto the drag balance and exposed to the air flow, only a portion 16 cm × 20 cm was made to oscillate. Time-resolved PIV data support the hot-wire and direct-drag measurements.

References

Akhavan R, Kamm R, Shapiro A (1991a) An investigation of transition to turbulence in bounded oscillatory Stokes flows Part 1. Experiments. J Fluid Mech 225:395–422

Akhavan R, Jung W, Mangiavacchi N (1993) Turbulence control in wall-bounded flows by spanwise oscillations. App Sci Res 51:299–303

Alfredsson PH, Örlü R, Kurian T, Fransson J, Segalini A, Ruedi JD, Talamelli A (2009) The diagnostic plot - a new way to appraise turbulent boundary-layer data. In: Eckhardt B (ed) Advances in Turbulence XII, Springer

Bradshaw P, Pontikos N (1985) Measurement in the turbulent boundary layer on an infinite-swept wing. J Fluid Mech 159:105–130

Choi K (2002) Near-wall structure of turbulent boundary layer with spanwise-wall oscillation. Phys Fluids 14(7):2530–2542

Choi K, Clayton B (2001) The mechanism of turbulent drag reduction with wall oscillation. Int J Heat Fluid Flow 22(1):1–9

Choi K, DeBisschop JR, Clayton B (1998) Turbulent boundary-layer control by means of spanwise-wall oscillation. AIAA Journal 36(7):1157–1163

Dearing S, Lambert S, Morrison J (2007) Flow control with active dimples. Aero J 111(1125):705–714

Dearing S, Morrison J, Iannucci L (2010) Electro-active polymer (eap) dimple actuators for flow control: Design and characterisation. Sensors and Actuators A: Physical 157:210–218

Du Y, Symeonidis V, Karniadakis G (2002) Drag reduction in wall-bounded turbulence via a transverse travelling wave. J Fluid Mech 457:1–34

Fernholz HH, Krause E, Nockemann M, Schober M (1995) Comparative measurements in the canonical boundary layer at $Re_{\delta2} < 6 \times 10^4$ on the wall of the DNW. Phys Fluids A 7:1275–1281

Gouder K (2011) Turbulent Friction Drag Reduction Using Electroactive Polymer Surfaces. PhD thesis, Imperial College London

Il-Choi J, Xu C, Sung H (2002) Drag reduction by spanwise wall oscillation in wall-bounded turbulent flows. AIAA Journal 40(5):842–850

Jung W, Mangiavacchi N, R A (1992) Suppression of turbulence in wall-bounded flows by high-frequency spanwise oscillations. Phys Fluids A 4(8):1605–1607

Kamphuis J (1975) Friction factor under oscillatory waves. J Waterways, Port Coastal Engineering, Div ASCE 101:135–144

Kofod G (2001) Dielectric elastomer actuators. PhD thesis, The Technical University of Denmark

Laadhari F, Skandaji L, Morel R (1994) Turbulence reduction in a boundary layer by a local spanwise oscillating surface. Phys Fluids 6(10):3218–3220

Pelrine R, Kornbluh R, Joseph J, Chiba S (1997) Electrostriction of polymer films for microactuators. IEEE 0-7803-3744-1:238–243

Potter M, Gouder K, Morrison J (2011) A numerical model for electro-active polymer actuators with experimental validation. Sensors and Actuators A: Physical 170:121–130

Quadrio M, Ricco P (2003) Initial response of a turbulent channel flow to spanwise oscillation of the walls. J Turb 4(007)

Quadrio M, Ricco P (2004) Critical assessment of turbulent drag reduction through spanwise wall oscillations. J Fluid Mech 521:251–271

Quadrio M, Sibilla S (2000) Numerical simulation of turbulent flow in a pipe oscillating around its axis. J Fluid Mech 424:217–241

Quadrio M, Viotti C, Luchini P (2007) Skin-friction drag reduction via steady streamwise oscillations of spanwise velocity. In: Palma JMLM, Silva Lopez A (eds) Advances in Turbulence XI, Springer

Quadrio M, Ricco P, Viotti C (2009) Streamwise-travelling waves of spanwise wall velocity for turbulent drag reduction. J Fluid Mech 627:161–178

Ricco P, Quadrio M (2007) Wall-oscillation conditions for drag-reduction in a turbulent channel flow. Int J Heat Fluid Flow 29(4):891–902

Ricco P, Wu S (2004) On the effects of lateral wall oscillations on a turbulent boundary layer. Exp Thermal Fluid Sci 29:41–52

Schlichting H (1968) Boundary Layer Theory, 6th edn. McGrawHill Book Company, New York

Schoppa W, Hussain F (1998) A large-scale control strategy for drag reduction in turbulent boundary layers. Phys Fluids 10(5):1049–1051

Zhao H, Wu JZ, Luo JS (2004) Turbulent drag reduction by travelling wave of flexible wall. Fluid Dynamics Research 34:175–198